6-5-2006

Role of Beat Noise in Limiting the Sensitivity of Optical Coherence Tomography

Richard C. Haskell
Harvey Mudd College

David Liao
Harvey Mudd College

Adam E. Pivonka
Harvey Mudd College

Tera L. Bell
Harvey Mudd College

Brendan R. Haberle
Harvey Mudd College

See next page for additional authors

Authors

Richard C. Haskell, David Liao, Adam E. Pivonka, Tera L. Bell, Brendan R. Haberle, Barbara M. Hoeling, and Daniel C. Petersen

Role of beat noise in limiting the sensitivity of optical coherence tomography

**Richard C. Haskell, David Liao, Adam E. Pivonka, Tera L. Bell, Brendan R. Haberle,
Barbara M. Hoeling, and Daniel C. Petersen**

Department of Physics, Harvey Mudd College, Claremont, California 91711

The sensitivity and dynamic range of optical coherence tomography (OCT) are calculated for instruments utilizing two common interferometer configurations and detection schemes. Previous researchers recognized that the performance of dual-balanced OCT instruments is severely limited by beat noise, which is generated by incoherent light backscattered from the sample. However, beat noise has been ignored in previous calculations of Michelson OCT performance. Our measurements of instrument noise confirm the presence of beat noise even in a simple Michelson interferometer configuration with a single photodetector. Including this noise, we calculate the dynamic range as a function of OCT light source power, and find that instruments employing balanced interferometers and balanced detectors can achieve a sensitivity up to six times greater than those based on a simple Michelson interferometer, thereby boosting image acquisition speed by the same factor for equal image quality. However, this advantage of balanced systems is degraded for source powers greater than a few milliwatts. We trace the concept of beat noise back to an earlier paper [J. Opt. Soc. Am. **52**, 1335 (1962)]. © 2006 Optical Society of America

OCIS codes: 030.4280, 110.4280, 120.3180, 170.4500.

1. INTRODUCTION

The sensitivity of an optical coherence tomography (OCT) instrument is the critical factor in determining the trade-off between image quality and image acquisition speed. OCT sensitivity is a measure of the smallest sample reflectivity or backscattering cross section that can be resolved, and is typically defined to be the variance of the instrument noise. Early OCT researchers[1–3] found it convenient to measure instrument noise with respect to a standard OCT signal and chose the signal returned from a perfectly reflecting mirror, the maximum achievable signal, as the standard. They defined the signal-to-noise ratio (SNR) as

$$\text{SNR} = \frac{\text{mean-square fringe amplitude from a mirror}}{\text{variance of photon and detector noise}},$$

(1)

where the denominator is small when the sensitivity of the instrument is high. The SNR as defined in Eq. (1) is also the square of the dynamic range (DR). We prefer to work with the DR parameter, although the SNR as defined in Eq. (1) can and has been used to discuss the sensitivity of OCT.

Often the noise in the denominator of Eq. (1) is measured without a sample, so that the noise is due to photon noise in the reference beam and thermal noise in the detector. Unfortunately this practice ignores the contribution of beat noise, which arises from incoherent light backscattered from the sample, i.e., light backscattered from outside the OCT coherence volume. During the imaging of typical biological tissue, the incoherent power backscattered from tissue can be as much as 2–3 orders of magnitude greater than the coherent power. (See Appendix A for a justification of this statement.) The theoretical results presented in Sections 2 and 4 show that this incoherent light and the associated beat noise severely limit the DR at source powers above 10 mW. Our results confirm earlier reports[4–6] that beat noise plays a critical role in limiting the DR of OCT instruments utilizing balanced interferometers and balanced detection. In Section 3 we report the first—to our knowledge—experimental confirmation of the presence of beat noise in a simple Michelson interferometer-based OCT instrument utilizing a single photodetector. We conclude that an accurate measure of OCT sensitivity must include all sources of noise present under normal OCT imaging conditions, including beat noise.

One of the goals of OCT instrument design has been to achieve shot-noise-limited detection in the expression for the SNR in Eq. (1); i.e., the noise in the denominator of Eq. (1) should be dominated by fundamental photon shot noise.[1] In this case, photon bunching, sometimes referred to as excess photon noise, would be less than or equal to shot noise. When light source powers greater than 1 mW are used, Bose–Einstein photon bunching typically dominates photon noise. At these higher source powers, Sorin and Baney[1] suggested attenuating the reference beam to reduce photon bunching, leaving primarily shot noise.

Unfortunately, attenuating the reference beam is wasteful of photons, and the use of balanced interferometers and balanced detection has become a popular alternative. Rollins *et al.*[7] used balanced detectors to cancel photon bunching and other fluctuations in light source intensity, sometimes referred to collectively as relative intensity noise. However, Takada[4] has shown that some photon bunching, referred to as beat noise, is not eliminated by balanced detection. Yoshino *et al.*[8] have demonstrated that the beating of different frequencies within

the source spectrum generates the usual photon bunching, and that interference between the partially coherent beams returned from the two arms of a Michelson interferometer results in an additional beat noise term and hence additional photon bunching. It is this additional beat noise term that is not eliminated by balanced detection. Our results presented in Section 4 indicate that the effectiveness of balanced detection is substantially reduced by this additional beat noise term for source powers above a few milliwatts.

Several research groups[5,6,9] have studied improvements in OCT sensitivity achieved with balanced interferometer configurations. For example, a balanced Mach–Zehnder interferometer can be used instead of an unbalanced Michelson interferometer so that photons from the OCT broadband light source are used more efficiently.[9] Rollins *et al.*[7] employed both a balanced interferometer configuration and balanced detectors in a so-called dual-balanced OCT instrument for use in real-time endoscopic OCT imaging of the gastrointestinal tract. Our theoretical study reported in Sections 2 and 4 suggests that dual-balanced design, with typical values for instrument parameters, can achieve at most a factor of 6 improvement in image acquisition speed while holding image quality constant. However, the presence of beat noise degrades this improvement factor when light source powers exceed a few milliwatts.

The recent development of Fourier-domain (or frequency-domain) OCT (FD-OCT),[10,11] sometimes referred to as spectral-domain OCT,[12] has provided an additional boost in sensitivity over conventional time-domain OCT (TD-OCT). Two different implementations of FD-OCT are emerging as most popular.[11] In the first, a broadband light source illuminates the interferometer input, and a spectrometer with a detector array is placed at the output. The light source power returned from the sample and reference arms is distributed over a large number of detectors operating in parallel in the array, reducing the power on each detector and allowing it to operate in the Poisson shot-noise regime. In this case, both the usual Bose–Einstein photon bunching and the additional beat noise are negligible. In the second implementation, a narrowband laser illuminates the interferometer, and the laser wavelength is swept quickly through a broad spectral range. The fringes at the interferometer output are recorded by a single detector. While the laser output power may be substantial, the laser is a coherent source, not a thermal source, and hence its output beam does not exhibit photon-bunching fluctuations. The laser pumping mechanism may impart relative intensity noise, but this can be eliminated with balanced detectors. Both implementations of FD-OCT can be free of photon bunching and hence escape the limitations described in the present paper. However, FD-OCT cannot accommodate focus tracking because all sample depths are probed simultaneously. When good lateral resolution is required throughout the depth of the sample, and when real-time acquisition rates are not essential, the TD-OCT method of *en face* scanning optical coherence microscopy may be the technique of choice. In these cases, the effects of photon bunching and beat noise on sensitivity become important for optimal image acquisition.

2. DYNAMIC RANGE

The DR of an OCT instrument can be defined as the ratio of the fringe amplitude originating from the surface of a mirror to the rms noise at the output of the instrument under typical imaging conditions. The DR is the square root of the SNR defined in Eq. (1):

$$\text{DR} = \sqrt{\text{SNR}} = \frac{\text{rms fringe amplitude from a mirror}}{\text{rms detector and photon noise}}$$

$$= \frac{F \eta_h \sqrt{P_\text{ref} P_\text{coh}}}{\text{rms noise}}. \tag{2}$$

The fringe amplitude in the numerator of Eq. (2) is proportional to the square root of the product of the reference power P_ref and the power coherently reflected from the mirror P_coh. The heterodyne efficiency η_h and the signal analysis factor F are each approximately equal to 1.[13] The rms noise in the denominator of Eq. (2) should be representative of instrument noise during imaging of tissue.

We shall evaluate the rms noise of an OCT instrument for balanced and unbalanced configurations, and then calculate the DR for each configuration with the help of Eq. (2). Our results are obtained for optimized OCT instruments, which means that, for Michelson interferometers, the reference beam power is attenuated to maximize the DR for a given light source power.[1,13] Similarly in balanced systems, the cross efficiency (splitting ratio) of the primary fiber coupler is adjusted to maximize the DR for a given light source power.

A. Michelson Interferometer

Figure 1 is a schematic of the most common example of an unbalanced OCT system. The variance of the noise in this system is given by

$$\langle (\Delta P_\text{Michelson})^2 \rangle = \underbrace{(\text{NEP})^2 (\text{BW})}_{\text{thermal noise of detector}}$$

$$+ \underbrace{(2 \; \text{BW} \; e/\mathfrak{R})(P_\text{ref} + P_\text{incoh})}_{\text{photon Poisson shot noise}}$$

$$+ \underbrace{(\text{BW} \; \tau_\text{coh})(1 + \text{Pol}^2)(P_\text{ref} + P_\text{incoh})^2}_{\text{Bose–Einstein photon bunching}}$$

$$+ \underbrace{(\text{BW} \; \tau_\text{coh})(1 + \text{Pol}^2)2P_\text{ref} + P_\text{incoh}}_{\text{beat noise}}. \tag{3}$$

The first term on the right side of Eq. (3) is the thermal noise of the photodetector. NEP is the noise-equivalent power of the detector in $\text{W/Hz}^{1/2}$, and BW is the bandwidth of the analog and digital signal-processing path-
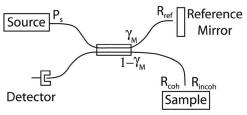

Fig. 1. Schematic of an unbalanced Michelson interferometer configuration. A single 2×2 fiber coupler is used with a splitting ratio of γ_M (chosen equal to $\frac{1}{2}$ for optimized performance). A single photodetector samples the interference fringes.

way. The second term is the photon Poisson shot noise,[14–16] where e is the electron charge and $\mathfrak{R}$ is the responsivity of the detector in A/W; P_{incoh} is the power returned from the sample arm that is incoherent with the reference beam, e.g., light backscattered from tissue (or the sample fiber tip) outside the coherence volume. (Actually, the P_{incoh} and P_{ref} beams are partially coherent, in the sense that narrow bands of wavelengths in the two beams can interfere, although the sum of these interference terms over all wavelengths goes nearly to zero.) When typical biological tissue is imaged, P_{incoh} is much greater than P_{coh} (see Appendix A); therefore we have neglected P_{coh} with respect to P_{incoh} and P_{ref} in Eq. (3). The third term is the Bose–Einstein photon-bunching term,[14–16] sometimes called excess photon noise, where τ_{coh} is the coherence time of the OCT light source. The factor $(1+\text{Pol}^2)$ accounts for the state of polarization of the OCT light source; Pol=0 corresponds to unpolarized light, and Pol=1 indicates plane-polarized light. The fourth term is the additional beat noise first derived by Mandel in 1962.[17] The beat noise term is equal in magnitude but distinct from the cross term in the usual photon-bunching term, the third term in Eq. (3). Beat noise arises because two partially coherent beams (P_{ref} and P_{incoh}), rather than a single thermal field, are incident upon the detector. In a recent detailed derivation using classical waves, Yoshino *et al.*[8] demonstrate that this beat noise term is due to the changes in the total optical spectrum incident upon the photodetector resulting from the interference of the two partially coherent beams.

The beam powers in Eqs. (2) and (3) can be written in terms of the light source power P_s and the cross efficiency γ_M of the fiber splitter of the Michelson interferometer:

$$P_{\text{ref}} = P_s \gamma_M (1 - \gamma_M) R_{\text{ref}}, \quad P_{\text{coh}} = P_s \gamma_M (1 - \gamma_M) R_{\text{coh}},$$

$$P_{\text{incoh}} = P_s \gamma_M (1 - \gamma_M) R_{\text{incoh}}, \tag{4}$$

where R_{ref} is the effective reflectivity of the reference mirror (including perhaps a neutral-density filter), R_{coh} is the cumulative reflectivity of scatterers in the coherence volume (the surface of a mirror for our present studies), and R_{incoh} is the cumulative reflectivity of scatterers outside the coherence volume. The dynamic range of the Michelson configuration is optimized by choosing $\gamma_M = 1/2$. We also reduce the value of R_{ref} to maximize the DR for a given light source power.[1,13]

B. Balanced Configuration

We now examine the noise of the balanced system shown in Fig. 2. This system is similar to the balanced system denoted as "Ai" by Rollins and Izatt,[5] but our balanced system employs two optical circulators for conceptual simplicity. The design of Fig. 2 utilizes a balanced interferometer and balanced detection. The noise variance of this system can be expressed as[4–6]
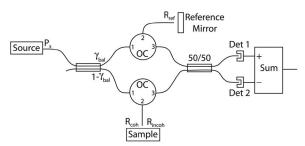

Fig. 2. Schematic of a dual-balanced OCT configuration. Two 2×2 fiber couplers are used; the primary coupler has a splitting ratio of γ_{bal} while the second coupler sends 50% to each detector. Two optical circulators (OC) are employed, one in the sample arm and one in the reference arm. Typically light is coupled from port 1 to port 2 or from port 2 to port 3 with ~85% efficiency. The outputs of two balanced detectors are subtracted to reject common-mode intensity noise.

$$\langle(\Delta P_{\text{bal}})^2\rangle = \underbrace{(\text{NEP}_{\text{dual}})^2(\text{BW})}_{\text{thermal noise of detectors}} + \underbrace{(2\ \text{BW}\ e/\mathfrak{R})(P_{\text{ref}} + P_{\text{incoh}})}_{\text{photon Poisson shot noise}}$$
$$+ \underbrace{(\text{BW}\ \tau_{\text{coh}})(1 + \text{Pol}^2)2P_{\text{ref}}P_{\text{incoh}}}_{\text{beat noise}}. \tag{5}$$

In Eq. (5), P_{ref} and P_{incoh} are the sum of the reference and incoherent powers, respectively, which are incident upon the two detectors. Here, NEP_{dual} is $\sqrt{2}$ times NEP in Eq. (3). The first term in Eq. (5) is the thermal detector noise, the second is the photon Poisson shot noise, and the last term is the beat noise. The Bose–Einstein photon-bunching term in Eq. (3) has been eliminated by the balanced detection circuitry included in Fig. 2, but the additional beat noise term survives.[4]

The beam powers in Eqs. (2) and (5) can be written in terms of the source power P_s and the cross efficiency γ_{bal} of the fiber splitter of the balanced configuration:

$$P_{\text{ref}} = P_s \gamma_{\text{bal}} T_{\text{circ}}^2 R_{\text{ref}}, \quad P_{\text{coh}} = P_s (1 - \gamma_{\text{bal}}) T_{\text{circ}}^2 R_{\text{coh}},$$

$$P_{\text{incoh}} = P_s (1 - \gamma_{\text{bal}}) T_{\text{circ}}^2 R_{\text{incoh}}. \tag{6}$$

Here, T_{circ} is the coupling efficiency (typically ~0.85, see also Ref. 5) between successive ports of an optical circulator. Equations (6) are analogous to Eqs. (4) for the Michelson configuration.

The advantage of the balanced configuration is that the coupling efficiency of the fiber splitter can be varied to direct more light to the sample while keeping the reference reflectivity at its maximum (optimum) value, thus maximizing the DR.[4–6]

3. BEAT NOISE IN A MICHELSON INTERFEROMETER

Equation (3) describes the noise in the simple OCT instrument shown in Fig. 1. The last term in Eq. (3), the beat noise term, appears in a form that has been simplified considerably from Eq. (19) of Mandel's 1962 paper.[17] In Appendix B of this paper, we outline the derivation of our Eq. (3) starting with Mandel's Eq. (19), focusing particular attention on the beat noise term, the last term in our Eq. (3). It is reassuring that the expression derived recently by Yoshino *et al.*[8] for beat noise at the output of a
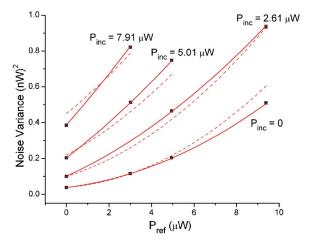
Fig. 3.   (Color online) Measured noise variance at the output of an OCM as a function of P_{ref} and P_{incoh}. The OCM instrument is based on a simple Michelson interferometer design, as illustrated in Fig. 1. The 12 data points (black squares, with error bars approximately the size of the squares) are fitted to the form of expression (7): $A+B(P_{ref}+P_{incoh})+C(P_{ref}+P_{incoh})^2+CDP_{ref}P_{incoh}$. The solid curves are the fitted curves yielding a reduced chi square of 0.60 (77% chance of exceeding). The fitted value of $D=2.04\pm0.10$ is consistent with the integer 2 in the last term of Eq. (3). The dashed curves are the best fit to the form of expression (7) without the beat noise term (the last term) and yield a reduced chi square of 113. The beat noise term is clearly needed to describe the data adequately.

Table 1. Results of Fitting the Data in Fig. 3 to the Functional Form of Expression (7)

Fitting Parameter	Expression from Eq. (3)	Fitted Value
A	$(NEP)^2(BW)$	$(38.0\pm0.4)\times10^{-3}$ $(nW)^2$
B	$2(BW)e/\Re$	$(14.4\pm0.3)\times10^{-3}$ $(nW)^2/\mu W$
C	$(BW)\tau_{coh}(1+Pol^2)$	$(3.77\pm0.07)\times10^{-3}$ $(nW)^2/(\mu W)^2$
D	2	2.04 ± 0.10

Michelson interferometer reduces, in the limit of large path difference, to our Eq. (3). However, some treatments[5,6] of the noise in a simple Michelson-based OCT instrument have omitted this beat noise term entirely. Given these discrepancies in the literature, we thought it important to verify experimentally the form of Eq. (3).

In this experiment, an *en-face* scanning, three-dimensional, optical coherence microscope (OCM) operating at 850 nm was used to image a mirror surface. The OCM instrument is based on a simple Michelson interferometer with a single photodetector, as depicted schematically in Fig. 1. The details of the instrument have been described previously.[13,18,19] The equal-path-length position in the sample arm was kept 3 mm above the surface of the mirror, so that all light returned from the sample arm came from outside the coherence volume. (We show in Appendix C of this paper that the expected noise is the same regardless of whether the backscattered light in the sample arm comes from a single mirror surface or from multiple scatterers outside the coherence volume.) The position of the focused waist of the sample beam was varied from 100 to 200 μm above the mirror surface so that the incoherent power P_{incoh} decreased correspondingly

due to the confocal rejection ratio of the OCM instrument. A series of neutral-density filters were inserted into the reference arm retroreflector to vary the reference arm power P_{ref}.

The beat noise term predicted by Eq. (3) can be as much as one third of the total noise variance when $P_{incoh}\approx P_{ref}$ and both are sufficiently large that the photon shot noise and the thermal detector noise are negligible. The noise variance was measured for several different values of P_{ref} and P_{incoh} that satisfied these conditions. A composite plot of the data is presented in Fig. 3. The data are fit to the form of Eq. (3):

$$A + B(P_{ref} + P_{incoh}) + C(P_{ref} + P_{incoh})^2 + CDP_{ref}P_{incoh}.$$
$$(7)$$

The fitted values for A, B, C, and D are listed in Table 1, and the fitted curves appear in Fig. 3 as the solid curves. The reduced chi square associated with the fit is 0.60 (77% chance of exceeding). Consistent values of A, B, and C are obtained when the subset of data with $P_{ref}=0$ is fitted and when the subset with $P_{incoh}=0$ is fitted. The fitted value of $D=2.04\pm0.10$ is consistent with the integer 2 in the beat noise term of Eq. (3). The dashed curves in Fig. 3 represent the best fit to the form of Eq. (3) but without the beat noise term and yield a reduced chi square of 113. Clearly the beat noise term is needed to describe the data adequately.

4. SIMULATION RESULTS
We have calculated the DR of the Michelson and balanced configurations by inserting the square root of Eqs. (3) and
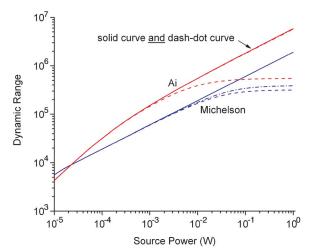

Fig. 4.   (Color online) Dynamic range (DR) plotted as a function of source power: The upper curves are values calculated for the balanced Ai configuration, and the lower curves are values for the unbalanced Michelson configuration. The solid curves are values calculated assuming no incoherent light backscattered from the sample path ($R_{incoh}=0$), while the dashed curves are for $R_{incoh}=3.5\times10^{-4}$, a typical value for tissue. The dashed–dotted curves are calculated assuming $R_{incoh}=3.5\times10^{-4}$, but with the beat noise terms omitted from Eqs. (3) and (5). (The Ai dashed–dotted and solid curves are superposed and are barely distinguishable.) Note that the beat noise term accounts for essentially all of the reduction in the DR of the Ai system as R_{incoh} changes from 0 to 3.5×10^{-4}, while approximately one third of the reduction in the Michelson is due to beat noise. Typical values for source powers range from 1 to 20 mW.
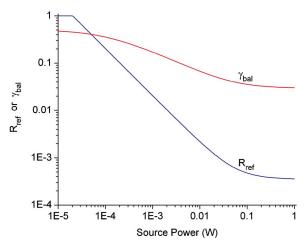
Fig. 5. (Color online) Values for the optimal reference reflectivity in Michelson configurations and values for the optimal fiber–splitter ratio in balanced Ai configurations, plotted as a function of source power. With higher source powers in Michelson systems, lower reference reflectivities are used to reduce Bose–Einstein photon bunching and optimize the DR. With higher source powers in balanced Ai configurations, more power is diverted from the reference arm (lower γ_{bal}) to the sample arm to optimize the DR. Note that for very low source powers, the Michelson DR is maximized with the maximum reference reflectivity ($R_{\mathrm{ref}} = 1$).

Table 2. Values for Parameters Used to Calculate the Data for Figs. 4–6

Parameter	Symbol and Value
Signal-processing factor	$F = 1.175$
Heterodyne efficiency	$\eta_h = 1.0$
Noise-equivalent power	NEP $= 1.4$ pW/Hz$^{1/2}$
Noise-equivalent power of dual detectors	NEP$_{\mathrm{dual}} = 2.0$ pW/Hz$^{1/2}$
Bandwidth of filter	BW $= 30$ kHz
Detector responsivity	$\mathfrak{R} = 0.95$ A/W
Source coherence time	$\tau_{\mathrm{coh}} = 76$ fs
Sample mirror reflectivity[a]	$R_{\mathrm{coh}} = 0.35$
Incoherent reflectivity	$R_{\mathrm{incoh}} = 0$ or 3.5×10^{-4}
Reference mirror reflectivity[a,b]	$R_{\mathrm{ref}} = 0.38$
Michelson splitting ratio	$\gamma_M = 1/2$
Circulator efficiency	$T_{\mathrm{circ}} = 0.85$
Polarization of light	Pol $= 0$

[a]Effective mirror reflectivity includes losses coupling back into the optical fiber.

[b]Balanced system only. For the Michelson system, R_{ref} is varied to maximize the DR.

(5), respectively, into the denominator of Eq. (2). The results for the DR are plotted in Fig. 4 as a function of light source power P_s. Typical values for the source power range from 1 to 20 mW.

For each value of the light source power, the value for R_{ref} in the Michelson configuration has been optimized to maximize the DR. Similarly, for each value of the source power, the cross efficiency γ_{bal} of the primary fiber coupler in the balanced configuration of Fig. 2 has been optimized to maximize the DR. These optimal values for R_{ref} and γ_{bal} are plotted in Fig. 5 as a function of source power. The values of the parameters used to calculate the DR are listed in Table 2. These are typical values for an OCT instrument operating at 1300 nm.

For the solid curves in Fig. 4, the power backscattered by tissue outside the coherence volume is neglected ($R_{\mathrm{incoh}} = 0$). Notice that in this unrealistic situation the DR for both designs rises without limit (solid curves) and that the asymptotic slopes are equal. This results in an asymptotic improvement factor of ~ 3.1 for the balanced Ai configuration over the Michelson interferometer. Note also that the Michelson configuration is apparently superior in the limit of very low source powers where the thermal detector noise in Eqs. (3) and (5) dominates. This is simply due to the fact that the Ai configuration employs two detectors as opposed to the Michelson's single detector. As a result, the total variance of thermal detector noise in the Ai dual-detector system is twice the thermal noise variance in the Michelson single detector. For the same reason, the NEP of the balanced Ai detectors is $\sqrt{2}$ times greater than the NEP for the single Michelson detector (see Table 2). Hence the Ai noise is greater when detector noise dominates, so at low source powers in Fig. 4, the curve for the Ai DR lies below that for the Michelson DR.

For the dashed curves in Fig. 4, R_{incoh} is assigned the value 3.5×10^{-4} that is typical for the imaging of biological tissue. The resulting power backscattered by the sample increases photon bunching and generates beat noise, leading to a leveling off of the DR for both balanced and unbalanced configurations. This effect has been reported previously, especially for balanced configurations.[4,6] The dashed–dotted curves in Fig. 4 are calculated with $R_{\mathrm{incoh}} = 3.5 \times 10^{-4}$ but without the beat noise terms in Eqs. (3) and (5). The dashed–dotted curve for the balanced Ai configuration lies on top of and is barely distinguishable from the solid curve ($R_{\mathrm{incoh}} = 0$), but differs slightly due to a small additional contribution from the backscattered sample light in the Poisson shot-noise term. Nearly all of the reduction in DR for the Ai configuration in going from the solid curve ($R_{\mathrm{incoh}} = 0$) to the dashed curve ($R_{\mathrm{incoh}} = 3.5 \times 10^{-4}$, including beat noise) is due to beat noise. In contrast, the dashed–dotted curve for the Michelson system is clearly visible in Fig. 4, and indicates that approximately one third of the reduction in DR is due to beat noise (source power $P_s \sim 10$ mW), while approximately two thirds is due to additional photon bunching from the backscattered sample light.

The ratio of the DR for the balanced Ai configuration to that for the Michelson interferometer is plotted in Fig. 6 as a function of source power. The solid curve is calculated with $R_{\mathrm{incoh}} = 0$, i.e., neglecting incoherent light backscattered from the sample. The dashed curve is calculated with $R_{\mathrm{incoh}} = 3.5 \times 10^{-4}$, a typical value for tissue, and shows the advantage of the balanced system to peak with a ratio of ~ 2.5 at a source power of 3 mW. At this source power, the improvement in SNR is $(2.5)^2 \approx 6$, enabling an image acquisition speed six times faster for the same image quality. At a higher source power of 30 mW, the advantage of the balanced system has fallen to a factor of 2.0 in DR or 4.0 in SNR.

The dashed–dotted curve in Fig. 6 illustrates the additional DR degradation introduced into the Michelson system by beat noise. In constructing the dashed–dotted curve, the DR values for the Ai configuration include the beat noise term in Eq. (5), but the DR values for the Mich-
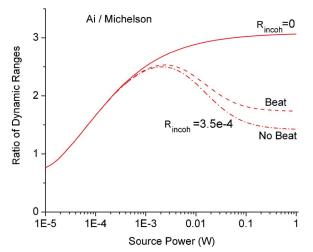
Fig. 6. (Color online) Improvement in the DR of the balanced Ai design over that of the Michelson configuration is plotted as a function of source power. The solid curve is calculated neglecting the incoherent light backscattered from the sample ($R_{incoh}=0$), while the dashed curve assumes $R_{incoh}=3.5\times10^{-4}$, a typical value for tissue. The dashed curve peaks at a value of 2.5 for approximately 3 mW of source power. The dashed–dotted curve is calculated with $R_{incoh}=3.5\times10^{-4}$ but without the beat noise term in Eq. (3). The dashed curve (with beat noise in the Michelson) falls above the dashed–dotted curve (no beat noise in the Michelson) because beat noise degrades the performance of the Michelson configuration.

elson system omit the beat noise term in Eq. (3). Researchers that have not included beat noise in their analysis of Michelson systems[5,6,20,21] have overstated the performance of these Michelson systems.

5. CONCLUSIONS

The phenomenon of beat noise was first discussed in connection with the Alford and Gold effect in 1962.[17] Mandel described it as an intensity correlation effect. Indeed, the origin of beat noise is fundamentally the same as that of Bose–Einstein photon bunching, and the approximate expression for beat noise, the last term in Eq. (3), is the same as the cross term in the photon-bunching expression, the third term in Eq. (3).

The most striking effect of beat noise in OCT is its contribution to the upper limit on the DR at high source powers. The curves in Fig. 4 begin to bend over and flatten out at source powers as low as 10 mW. This flattening is almost entirely due to beat noise in the case of the balanced Ai system, as noted by previous researchers.[4,6,22] In Michelson systems the flattening stems mostly from photon bunching, with a significant contribution (30%–40%) from beat noise. (Beat noise accounts for 40% of the reduction in DR at a source power of 1 mW and for 31% at a source power of 20 mW.)

It is interesting to note that the improvement factor in DR for the balanced Ai system over a Michelson interferometer is affected only modestly by photon bunching and beat noise due to backscattered sample light. For example, the DR improvement ratio is roughly 2.7 with $R_{incoh}=0$ and a source power of 3 mW, and is reduced slightly to 2.5 with $R_{incoh}=3.5\times10^{-4}$. However, it should be noted that this predicted improvement in DR assumes

ideal behavior of fiber splitters and balanced detectors. Rosa and Podoleanu[22] show that the dependence on wavelength of the fiber–splitter ratio can lead to a significant reduction in the DR of dual-balanced systems when broadband light source ($\Delta\lambda>100$ nm) are used.

It is clear that an ideal dual-balanced OCT configuration can provide a factor of up to 6 increase in image acquisition speed. Balanced detectors and optical circulators add complexity and expense to the instrument, but the importance of real-time or video-rate imaging may well justify the extra effort.

APPENDIX A

During the imaging of typical biological tissue, the incoherent power backscattered from tissue can be as much as 2–3 orders of magnitude greater than the coherent power. This assertion follows from OCT single-scattering theory, and we present in this appendix the logical arguments that lead to this conclusion.

The coherent power backscattered from a depth z in the sample is attenuated by the product of two factors: (1) the attenuation of the incident beam as it travels down to depth z and (2) the attenuation of the backscattered light as it travels back up to the surface of the sample.

$$P_{coh} \approx P_0 \exp(-\mu_{attn}z)\mu_{back}\ell_{coh}\exp(-\mu_{attn}z), \quad (A1)$$

where $\mu_{attn}=1/\ell_{attn}$ is the attenuation coefficient of the tissue and is equal to the reciprocal of the attenuation length. The backscattering coefficient μ_{back} is a function of depth z and also has units of inverse length. The coherence length of the OCT light source is ℓ_{coh}.

The incoherent power backscatterd from the sample is the backscattered power integrated over all depths in the sample outside the coherence volume. If we assume μ_{back} is constant throughout the tissue sample, we can calculate the incoherent power as

$$P_{incoh} \approx \int_0^\infty P_0 \exp(-2\mu_{attn}z)\mu_{back}dz = P_0\mu_{back}\ell_{attn}/2.$$

$$(A2)$$

In approximation (A2) we have included the light backscattered from all sample depths, including those depths that lie in the coherence volume. In P_{incoh} this error includes the backscattered power that comprises P_{coh}. As we shall see, this is not a significant error.

The ratio of incoherent-to-coherent power is therefore

$$\frac{P_{incoh}}{P_{coh}} \approx \frac{\ell_{attn}}{2\ell_{coh}}\exp(2\mu_{attn}z). \quad (A3)$$

A typical attenuation coefficient for tissue is 5/mm, yielding an attenuation length of 200 μm. A typical coherence length for an OCT light source is 10 μm. If we consider a typical imaging depth of two attenuation lengths, we find for the ratio of incoherent-to-coherent power backscattered from the sample:

$$\frac{P_{\text{incoh}}}{P_{\text{coh}}} \approx \frac{200\ \mu\text{m}}{20\ \mu\text{m}} \exp(4) = 546. \tag{A4}$$

Of course if the coherence volume were positioned at a depth of three attenuation lengths, the ratio in approximation (A3) would be 4030. On the other hand, if the coherence volume were positioned at the tissue surface ($z = 0$), the ratio in approximation (A3) would be 10. Moreover the strong specular reflection from the air–tissue interface would enhance P_{coh}, and so the ratio would certainly be lower than 10. With such a strong fringe signal, our OCT noise analysis is not needed—the SNR when imaging the tissue surface is quite high. Our OCT noise analysis is most useful when the OCT fringe signal is weak, so we have taken an imaging depth of two attenuation lengths to be typical. Hence the ratio $P_{\text{incoh}}/P_{\text{coh}}$ is of the order of 100–1000.

APPENDIX B

Equation (3) in Subsection 2.A describes the variance of the noise at the output of the Michelson OCT system depicted in Fig. 1. The form of this equation follows from Eq. (19) of Mandel's 1962 paper on the Alford and Gold effect.[17] In this appendix, we outline the derivation of our Eq. (3) starting with Mandel's Eq. (19), focusing particular attention on the beat noise term, the last term in our Eq. (3).

Figure 1 in Mandel's paper[17] depicts two polarized, partially coherent beams incident upon a photodetector. The beams can be considered to be produced by the beam splitter in a Michelson interferometer with a path-length difference given by cT, where T is the time delay between the two beams. It is assumed that $T\Delta\nu \gg 1$, where $\Delta\nu$ is the spectral width of both beams, so that the beams are nearly incoherent. A narrowband electrical filter follows the photodetector and is centered at frequency ν_1 with a width of $\delta\nu$. It is also assumed that $T\delta\nu \gg 1$. (Typical values are $\delta\nu \sim 10^3 - 10^6$ Hz and $\Delta\nu \sim 10^{13} - 10^{15}$ Hz.) The mean-square signal $\overline{S_2^2}$ at the output of the electrical filter is given by Mandel's Eq. (19):

$$\overline{S_2^2} = \bar{\alpha}(\bar{I}_1 + \bar{I}_2) \int_{-\infty}^{\infty} |B(\nu)|^2 \mathrm{d}\nu \left\{ 1 + \bar{\alpha}(\bar{I}_1 + \bar{I}_2)\Psi_{44}^I(\nu_1) \right.$$
$$\left. \times \left[1 + \frac{2\bar{I}_1\bar{I}_2}{(\bar{I}_1 + \bar{I}_2)^2}\gamma_{12}^2(0)\cos(2\pi\nu_1 T) \right] \right\}. \tag{B1}$$

In Eq. (B1) [Mandel's Eq. (19)], the mean-square signal $\overline{S_2^2}$ is also the variance of the detector–filter output because the electrical filter blocks the dc component of the detector output. Hence $\overline{S_2^2}$ is the variance of the noise current, while our Eq. (3) describes the variance of the detector output in terms of equivalent optical power.

The parameter $\bar{\alpha}$ in Eq. (B1) is the mean quantum sensitivity of the detector averaged over the incident light spectrum, and $\bar{I}_1$ and $\bar{I}_2$ are the mean intensities of the two partially coherent beams incident upon the photodetector. $B(\nu)$ is the complex frequency response of the electrical filter, and $\int_{-\infty}^{\infty} |B(\nu)|^2 \mathrm{d}\nu = 2\delta\nu = 2\text{BW}$, where $\delta\nu$ is the bandwidth of the filter and is written as BW in our Eq. (3). $\Psi_{44}^I(\nu_1) \approx \Psi_{44}^I(0)$ is a measure of the coherence time of each beam [see Mandel's Eq. (12) and the text following], which we call τ_{coh} in our Eq. (3). The parameter $\gamma_{12}(0)$ is the degree of coherence of the two beams (at zero time delay), which we call the heterodyne efficiency and assign a value of approximately 1.

Expanding the parentheses in Eq. (B1), and substituting $\cos(2\pi\nu_1 T) \approx 1$ as well as the other approximations and identities discussed above, we can write Eq. (B1) as

$$\text{Var}(S_2) = 2\text{BW}(\bar{\alpha}\bar{I}_1 + \bar{\alpha}\bar{I}_2) + 2\text{BW}\tau_{\text{coh}}(\bar{\alpha}\bar{I}_1 + \bar{\alpha}\bar{I}_2)^2$$
$$+ 2\text{BW}\tau_{\text{coh}}2\bar{\alpha}\bar{I}_1\bar{\alpha}\bar{I}_2. \tag{B2}$$

Mandel has chosen units of photoelectrons per photon for the quantum sensitivity $\bar{\alpha}$ and units of photons per second for $\bar{I}$, so that $\bar{\alpha}\bar{I}$ is the number of electrons per second and hence has units of 1/s. Both sides of Eq. (B2) therefore have units of $1/\text{s}^2$. To convert to the units of effective optical power as in our Eq. (3), we must multiply $\bar{\alpha}\bar{I}$ by $e/\Re$, where e is the electron charge in coulombs and $\Re$ is the detector responsivity in A/W. Multiplying both sides of Eq. (B2) by $(e/\Re)^2$, and associating $(e/\Re)\bar{\alpha}\bar{I}_1$ with P_{ref} and $(e/\Re)\bar{\alpha}\bar{I}_2$ with P_{incoh},

$$\langle(\Delta P_{\text{Michelson}})^2\rangle = 2\text{BW}(e/\Re)(P_{\text{ref}} + P_{\text{incoh}}) + 2\text{BW}\tau_{\text{coh}}$$
$$\times (P_{\text{ref}} + P_{\text{incoh}})^2 + 2\text{BW}\tau_{\text{coh}}2P_{\text{ref}}P_{\text{incoh}}. \tag{B3}$$

It is important to note that Mandel considered two polarized beams falling on the detector. Therefore the leading factor of 2 in the second and third terms on the right-hand side of Eq. (B3) can be written as $(1 + \text{Pol}^2)$, where Pol = 1 corresponds to plane-polarized beams, and $P = 0$ corresponds to unpolarized beams, the case we consider in this paper.[13] Thermal detector noise must be added to Eq. (B3), so that we finally have

$$\langle(\Delta P_{\text{Michelson}})^2\rangle = (\text{NEP})^2(\text{BW}) + 2\text{BW}(e/\Re)(P_{\text{ref}} + P_{\text{incoh}})$$
$$+ \text{BW}\tau_{\text{coh}}(1 + \text{Pol}^2)(P_{\text{ref}} + P_{\text{incoh}})^2$$
$$+ \text{BW}\tau_{\text{coh}}(1 + \text{Pol}^2)2P_{\text{ref}}P_{\text{incoh}}, \tag{B4}$$

which is identical to Eq. (3).

APPENDIX C

In Section 3 we reported measurements of detector noise at the output of an OCM interferometer. In performing those measurements, we placed a mirror surface in the sample arm more than 100 coherence lengths away from the equal-path-length position (coherence volume) of the interferometer. Light backscattered from the mirror surface was incoherent with the beam reflected from the reference mirror, and hence no interference fringes were visible at the output of the interferometer. When imaging biological tissue, the incoherent light returning from the sample arm will presumably arise from a large number of randomly positioned scatterers, most of them located far outside the coherence volume. It is important to ask whether the data presented in Section 3 are relevant to

OCM imaging of tissue. Can Eq. (3) describe the detector noise variance measured from both types of samples? In addition, can Eq. (3) describe the detector noise variance measured with scatterers present in the coherence volume? In our discussion of Eq. (3) in Subsection 2.A, we mentioned our assumption that P_{coh} can be neglected with respect to P_{incoh} and P_{ref} when imaging tissue.

These questions can be answered with the help of results reported recently by Yoshino *et al.*[8] The contribution of spontaneous emission to the noise variance at the output of a Michelson interferometer is given by Yoshino's Eq. (22):

$$\sigma_{SE\text{-}SE}^2 \propto [3 + \text{sinc}^2(\pi B_0 \tau) + 4\,\text{sinc}(\pi B_0 \tau)\cos(\omega_0 \tau)]. \tag{C1}$$

[Note: there is a misplaced square bracket "]" at the end of Yoshino's Eq. (22), as becomes evident in reading the discussion immediately following Eq. (22).] In relation (C1), B_0 is the optical spectral width, ω_0 is the optical angular frequency, and τ is the delay time between the beams in the two arms of the Michelson interferometer. Our placement of a mirror surface many coherence lengths outside the coherence volume corresponds to taking the limit $B_0\tau \gg 1$, so that the square bracket in relation (C1) reduces to 3. We have explored the limit of $B_0\tau \gg 1$ in the full form of Yoshino's Eq. (22), adding thermal detector noise and Poisson (shot) photon noise, and have found that the results of Yoshino *et al.* are in agreement with our Eq. (3), which is valid for large path-length differences.

The form of relation (C1) allows us to treat the situation in which the reflectivity of the mirror surface is instead distributed among many scatterers that are located randomly outside the coherence volume. Provided that all scatterers are far from the coherence volume, the square brackets in relation (C1) reduce to approximately 3 for each scatterer, and the sum over all scatterers yields the same result as long as the cumulative reflectivity of the ensemble of scatterers is the same as the reflectivity of the single mirror surface; i.e., P_{incoh} is the same for both sample systems.

We can also treat the situation in which scatterers are randomly distributed throughout the sample, including near to and inside the coherence volume. Let us assume that the average density of scatterers is uniform, but that the scatterers are positioned randomly throughout the sample: far from, near to, and inside the coherence volume. Summing the contributions of scatterers at all depths in the sample requires that we sum relation (C1) over many random values of τ, weighting each contribution by the intensity of the coherent incident beam at the depth of the scatterer. Typically there is one dominant scatterer per coherence volume; if not, speckle becomes a real issue. It is possible, then, that a scatterer could be located in the center of the coherence volume (at $\tau=0$) so that the expression in square brackets in relation (C1) reaches its maximum value of 8. It is also possible that the scatterer could be located a quarter-wavelength away from the center of the coherence volume and yield a value of zero for the expression in square brackets. Yoshino *et al.*[8] point out that this latter result is sensible because when destructive interference yields zero signal at the

output of the interferometer, one would expect the variance of the output to be close to zero.

In summing relation (C1) over many random values of τ, it is clear that the third term in the square brackets will yield zero contribution. On the other hand, because $\int_{-\infty}^{+\infty}\text{sinc}^2(x)\mathrm{d}x = \pi$, the second term in the square brackets will increase the expression in the square brackets roughly by a factor of 2. In other words, the presence of scatterers in the coherence volume will increase the predicted noise variance. In particular, if the coherence volume resides on the air–tissue interface, the coherent backscattered power and the resulting fringe signal will be strong, and the noise variance will be increased significantly. However, when the fringe signal is strong, there is not much interest in the noise variance because the SNR is very high. When imaging tissue, it is more typical for the coherence volume to be located deep within the tissue, yielding a very weak fringe signal, in which case the noise variance is important. The scatterers in the coherence volume deep in the tissue will now be illuminated with a very attenuated incident beam, and their contributions to the sum over relation (C1) will be weighted very weakly. Thus, for conditions realized when imaging tissue, the presence of scatterers in the coherence volume does not alter significantly the expression for the noise variance described in Eq. (3). In summary, replacing the localized mirror surface with distributed scatterers makes little difference, as long as the scatterers inside the coherence volume do not dominate the backscattered light.

ACKNOWLEDGMENTS

REFERENCES

1. W. V. Sorin and D. M. Baney, "A simple intensity noise reduction technique for optical low-coherence reflectometry," IEEE Photon. Technol. Lett. **4**, 1404–1406 (1992).
2. E. A. Swanson, D. Huang, M. R. Hee, J. G. Fujimoto, C. P. Lin, and C. A. Puliafito, "High-speed optical coherence domain reflectometry," Opt. Lett. **17**, 151–153 (1992).
3. B. Bouma, G. J. Tearney, S. A. Boppart, M. R. Hee, M. E. Brezinski, and J. G. Fujimoto, "High-resolution optical coherence tomographic imaging using a mode-locked Ti:Al$_2$O$_3$ laser source," Opt. Lett. **20**, 1486–1488 (1995).
4. K. Takada, "Noise in optical low-coherence reflectometry," IEEE J. Quantum Electron. **34**, 1098–1108 (1998).
5. A. Rollins and J. Izatt, "Optimal interferometer designs for optical coherence tomography," Opt. Lett. **24**, 1484–1486 (1999).
6. A. Gh. Podoleanu, "Unbalanced versus balanced operation in an optical coherence tomography system," Appl. Opt. **39**, 173–182 (2000).
7. A. M. Rollins, R. Ung-arunyawee, A. Chak, R. C. K. Wong, K. Kobayashi, M. V. Sivak, Jr., and J. A. Izatt, "Real-time *in vivo* imaging of human gastrointestinal ultrastructure by use of endoscopic optical coherence tomography with a novel efficient interferometer design," Opt. Lett. **24**, 1358–1360 (1999).
8. T. Yoshino, M. R. Ali, and B. C. Sarker, "Performance

analysis of low-coherence interferometry, taking into consideration optical beat noise," J. Opt. Soc. Am. B **22**, 328–335 (2005).

9. B. E. Bouma and G. J. Tearney, "Power-efficient nonreciprocal interferometer and linear-scanning fiber-optic catheter for optical coherence tomography," Opt. Lett. **24**, 531–533 (1999).

10. R. Leitgeb, C. K. Hitzenberger, and A. F. Fercher, "Performance of Fourier domain vs. time domain optical coherence tomography," Opt. Express **11**, 889–894 (2003).

11. M. A. Choma, M. V. Sarunic, C. Yang, and J. A. Izatt, "Sensitivity advantage of swept source and Fourier domain optical coherence tomography," Opt. Express **11**, 2183–2189 (2003).

12. J. F. de Boer, B. Cense, B. H. Park, M. C. Pierce, G. J. Tearney, and B. E. Bouma, "Improved signal-to-noise ratio in spectral-domain compared with time-domain optical coherence tomography," Opt. Lett. **28**, 2067–2069 (2003).

13. B. M. Hoeling, A. D. Fernandez, R. C. Haskell, E. Huang, W. R. Myers, D. C. Petersen, S. E. Ungersma, R. Wang, M. E. Williams, and S. E. Fraser, "An optical coherence microscope for 3-dimensional imaging in developmental biology," Opt. Express **6**, 136–146 (2000).

14. L. Mandel and E. Wolf, *Optical Coherence and Quantum Optics* (Cambridge U. Press, 1995), Chap. 9.

15. P. R. Morkel, R. I. Laming, and D. N. Payne, "Noise characteristics of high-power doped-fibre superluminescent sources," Electron. Lett. **26**, 96–98 (1990).

16. H. Hodara, "Statistics of thermal and laser radiation," Proc. IEEE **53**, 696–704 (1965).

17. L. Mandel, "Interference and the Alford and Gold effect," J. Opt. Soc. Am. **52**, 1335–1340 (1962).

18. B. M. Hoeling, A. D. Fernandez, R. C. Haskell, and D. C. Petersen, "Phase modulation at 125 kHz in a Michelson interferometer using an inexpensive piezoelectric stack driven at resonance," Rev. Sci. Instrum. **72**, 1630–1633 (2001).

19. B. M. Hoeling, M. E. Peter, D. C. Petersen, and R. C. Haskell, "Improved phase modulation for an *en-face* scanning 3D optical coherence microscope," Rev. Sci. Instrum. **75**, 3348–3350 (2004).

20. H. D. Ford, R. Beddows, P. Casaubieilh, and R. P. Tatum, "Comparative signal-to-noise analysis of fibre-optic based optical coherence tomography systems," J. Mod. Opt. **52**, 1965–1979 (2005).

21. U. Sharma, N. M. Fried, and J. U. Kang, "All-fiber common-path optical coherence tomography: sensitivity optimization and system analysis," IEEE J. Sel. Top. Quantum Electron. **11**, 799–805 (2005).

22. C. C. Rosa and A. Gh. Podoleanu, "Limitation of the achievable signal-to-noise ratio in optical coherence tomography due to mismatch of the balanced receiver," Appl. Opt. **43**, 4802–4815 (2004).